catalysts

MDPI

Article

Construction of ZnS/$CoMoO_4$ Heterojunction for Boosted Visible-Light Photocatalytic Degradation of Methylene Blue

Teng Du [1,†], Zhen Wang [2,†], Huimin Zhang [1], Haiyang Wang [1,*], Shaofang Zheng [2], Yang Peng [1], Hairu Wang [1], Shuyue Du [3], Hongchang Qiao [2] and Yuzhen Zhao [1,*]

[1] Technological Institute of Materials & Energy Science (TIMES), Key Laboratory of Liquid Crystal Polymers Based Flexible Display Technology in National Petroleum and Chemical Industry, Xi'an Key Laboratory of Advanced Photo-Electronics Materials and Energy Conversion Device, School of Materials and New Energy, Xijing University, Xi'an 710123, China; 20230162@xijing.edu.cn (T.D.); huiminzhang0202@163.com (H.Z.); pengpy188@163.com (Y.P.); wanghairu725@163.com (H.W.)

[2] Shaanxi Experimental Center of Geological Survey, Shaanxi Institute of Geological Survey, Xi'an 710065, China; wangzwq@126.com (Z.W.); zheng2026syzx@163.com (S.Z.); hchqiao@163.com (H.Q.)

[3] School of Water Resources & Environmental Engineering, East China University of Technology, Nanchang 330013, China; shuyuedu0223@163.com

* Correspondence: 20200033@xijing.edu.cn (H.W.); zhaoyuzhen@xijing.edu.cn (Y.Z.)

† These authors contributed equally to this work.

Abstract

Effluents from the textile dyeing and printing industries are chemically complex and highly toxic, and synthetic dyes such as methylene blue (MB) are chemically stable and resistant to biological degradation, posing a persistent threat to aquatic ecosystems and human health. To address this challenge, a series of ZnS/$CoMoO_4$ heterojunction nanocomposites with ZnS loading fractions ranging from 5 to 50 wt% were constructed via a facile one-step hydrothermal route. The crystal phases, functional groups, surface chemical states, morphologies, pore textures, and optical/electrochemical properties of the products were interrogated by XRD, FT-IR, Raman, XPS, SEM, TEM-EDS mapping, N_2 physisorption, UV–vis DRS, EIS, and PL spectroscopy. XPS analysis demonstrates that coupling ZnS with $CoMoO_4$ establishes a directional ZnS → $CoMoO_4$ interfacial electron-transfer channel and simultaneously multiplies oxygen vacancies on the molybdate surface, which together accelerate the migration and separation of photogenerated carriers. Under visible-light irradiation ($\lambda \geq 420$ nm), all heterojunction samples outperformed the bare semiconductors, and the activity followed a volcano-type dependence on ZnS content. The 15 wt% ZnS/$CoMoO_4$ composite delivered the best performance, degrading 88.8% of MB within 120 min with a pseudo-first-order rate constant of 0.01595 min^{-1}, 2.58 and 1.49 times those of pristine ZnS and $CoMoO_4$, respectively, and it retained 82.2% degradation efficiency after five consecutive cycles. The enhancement is consistent with an S-scheme charge-transfer pathway at the ZnS/$CoMoO_4$ interface, an interpretation supported collectively by the element-specific interfacial binding-energy shifts, the multiplied oxygen vacancies, and the quenched photoluminescence of the composites. Unlike the physically mixed ZnS/$CoMoO_4$ analogue reported for hydrogen evolution, the in situ one-step hydrothermal construction studied here establishes an intimate, chemically contacted interface, and a systematic 5–50 wt% loading series resolves a volcano-type activity optimum. This work provides an experimental basis for the rational design of molybdate–sulfide heterojunction photocatalysts for dye wastewater remediation.

Keywords: ZnS/$CoMoO_4$; S-scheme heterojunction; photocatalysis; methylene blue; dye wastewater; one-step hydrothermal method

Check for updates

Academic Editor: Detlef W. Bahnemann

Received: 13 October 2026
Revised: 14 November 2026
Accepted: 16 November 2026
Published: 18 November 2026

Copyright: © 2026 by the authors. Licensee MDPI, Basel, Switzerland. This article is an open access article distributed under the terms and conditions of the Creative Commons Attribution (CC BY) license.

1. Introduction

Synthetic dyes are indispensable to modern textile dyeing and printing operations, yet a substantial fraction of these colorants escapes fixation and is discharged with the process water. The World Bank has estimated that textile dyeing and finishing account for roughly one-fifth of global industrial water pollution [1]. Beyond their intense coloration, dye molecules often carry aromatic azo, thiazine, or anthraquinone chromophores that suppress light penetration, hamper photosynthesis, deplete dissolved oxygen, and accumulate along food chains; some of them are mutagenic or carcinogenic [2,3]. Conventional treatments such as coagulation–flocculation, adsorption, and biological degradation either merely transfer dyes from the aqueous to the solid phase or fail to break down these recalcitrant molecules, frequently at the cost of secondary pollution [2,4]. Developing technologies that can thoroughly destroy dye pollutants under mild, economical, and sustainable conditions is therefore an urgent priority.

Semiconductor photocatalysis, a representative advanced oxidation process (AOP), harvests renewable solar energy to generate strongly oxidizing reactive oxygen species (ROS) such as hydroxyl (•OH) and superoxide ($\bullet O_2^-$) radicals, which can mineralize organic dyes into CO_2, H_2O, and small inorganic ions at ambient temperature and pressure without leaving secondary pollutants [4,5]. Since the landmark reports on TiO_2-based photoelectrochemistry and nitrogen-doped visible-light photocatalysis [6,7], the field has expanded explosively. The efficiency of photocatalytic degradation is governed collectively by light harvesting, the separation dynamics of photogenerated electrons and holes, and interfacial redox capability [5,8]; consequently, the rational design of efficient, stable, and inexpensive photocatalysts lies at the heart of practical dye wastewater treatment.

Zinc sulfide (ZnS) is a classic II–VI group semiconductor that has attracted long-standing interest in photocatalysis thanks to its rapid photogeneration of charge carriers, sufficiently negative conduction band (CB) potential, low cost, and low toxicity [8,9]. Nevertheless, its wide band gap (3.2–3.7 eV depending on polymorph and crystallite size) restricts the light response to the ultraviolet region, which contributes less than 5% of the solar spectrum, and its photogenerated electrons and holes recombine rapidly, severely limiting the quantum efficiency [8–10]. In addition, sulfide semiconductors are vulnerable to photocorrosion, in which valence-band holes oxidize S^{2-} species and leach Zn^{2+} into the solution; managing this degradation mode, together with the rapid bulk recombination characteristic of sulfide photocatalysts, remains a central challenge for sulfide-based photocatalysis [8,11]. Cobalt molybdate ($CoMoO_4$), a p-type narrow-band-gap transition-metal molybdate (≈1.8–2.8 eV), possesses abundant Co^{2+}/Co^{3+} and Mo^{4+}/Mo^{6+} redox couples and responds well to visible light; it has been investigated intensively for supercapacitors, electrocatalysis, and photocatalytic energy conversion [12–14]. Bare $CoMoO_4$, however, suffers from modest charge-carrier separation efficiency and only moderate photocatalytic activity toward organic dyes [14–16]. Given that the band edges of ZnS and $CoMoO_4$ are staggered, coupling the two semiconductors into an intimate heterojunction is a logical strategy: the built-in electric field formed at the phase boundary can drive directional migration and spatial separation of photogenerated carriers, while the narrow-gap component extends the spectral response into the visible region, cooperatively amplifying photocatalytic performance [8,17–20].

Heterojunction engineering—encompassing type-II, Z-scheme, and the newer S-scheme architectures—is now recognized as one of the most effective routes to accelerate charge separation while preserving strong redox power [18–21]. For ZnS-based systems, composites such as ZnS/g-C_3N_4 [22], ZnS/TiO_2 [23], ZnS/WO_3 [24,25], and other metal-sulfide junctions [11,24] display markedly promoted degradation of organic pollutants. For $CoMoO_4$-based systems, p–n ZnO/$CoMoO_4$ [15], g-C_3N_4/$CoMoO_4$ [26–28], and

carbon-quantum-dot-decorated $CoMoO_4$ [29] heterostructures similarly boost visible-light activity toward dyes, antibiotics, and hydrogen evolution. Very recently, a ZnS/CoMoO4 ball-and-rod composite prepared by physical mixing was reported for S-scheme photocatalytic hydrogen production [30], and photocatalytic nanoreactor design concepts together with anti-Stokes strategies have further enriched the toolbox for interfacial charge management [31,32]. To the best of our knowledge, however, a systematic study of ZnS/$CoMoO_4$ composites for the photocatalytic degradation of organic dyes—including the influence of the ZnS loading fraction on microstructure and degradation performance—has not been reported. This distinction matters. The composite of ref. [30] was obtained by physically mixing pre-formed ZnS and $CoMoO_4$ powders and was evaluated for hydrogen evolution, whereas the junction in the present work is constructed in situ during a one-step hydrothermal reaction. In situ growth produces a chemically contacted interface—reflected in element-specific XPS binding-energy shifts and in the multiplication of surface oxygen vacancies—and enables a systematic six-point loading series (5–50 wt%) that resolves a volcano-type activity dependence with an optimum at 15 wt% and quantifies the mitigation of ZnS photocorrosion over repeated cycles. Methylene blue is employed here as a common probe molecule, which facilitates direct comparison of our results with those reported in the literature, so that the results are directly comparable with the literature; the questions addressed are the composition–structure–performance relationship of the molybdate–sulfide couple and the visible-light stability of a sulfide photocatalyst, rather than the degradation of MB per se.

In this work, a series of ZnS/$CoMoO_4$ nanocomposites with ZnS mass fractions of 5, 10, 15, 20, 30, and 50 wt% were fabricated through a simple one-step hydrothermal process, and their phase composition, morphology, surface chemistry, and optical/electrochemical properties were systematically characterized by XRD, FT-IR, Raman, XPS, SEM, TEM-EDS mapping, N_2 physisorption, UV–vis DRS, EIS, and PL. Methylene blue (MB), a thiazine dye ubiquitous in textile effluents, was selected as the model pollutant to evaluate visible-light photocatalytic activity and to screen the optimal formulation. The interfacial charge-transfer behavior was interrogated by XPS binding-energy shifts, and an S-scheme mechanism for the enhanced activity is proposed. This study provides an experimental foundation for designing molybdate–sulfide heterojunction photocatalysts aimed at dye wastewater remediation.

2. Results and Discussion

2.1. Phase Structure

The crystalline phases of the as-prepared samples were identified by XRD (Figure 1a–c). For pristine ZnS (Figure 1a), diffraction peaks at 28.6°, 47.6°, and 56.4° are indexed to the (111), (220), and (311) planes of cubic sphalerite ZnS (JCPDS No. 01-0792); the absence of extraneous reflections confirms the formation of phase-pure ZnS [9,23]. For pristine $CoMoO_4$ (Figure 1b), all reflections match the standard pattern of monoclinic CoMoO4, including the (001), (−201), (021), (−311), (−131), (−222), (040), (−422), and (241) planes; the intense peak near 26.5° assigned to the (002) plane and the sharp peak profiles indicate a well-crystallized product [14,16,26]. In the XRD patterns of the ZnS/$CoMoO_4$ composites with different ZnS loadings (Figure 1c), both the (002) reflection of $CoMoO_4$ and the (111) reflection of ZnS are discernible, verifying that ZnS was successfully assembled onto the $CoMoO_4$ matrix and that the heterostructure was established. The intensity of the ZnS (111) peak grows progressively with increasing ZnS loading, while the $CoMoO_4$ reflections remain essentially unshifted, demonstrating that the introduction of ZnS does not disturb the host lattice; no impurity peaks appear, indicating high purity of the composites.

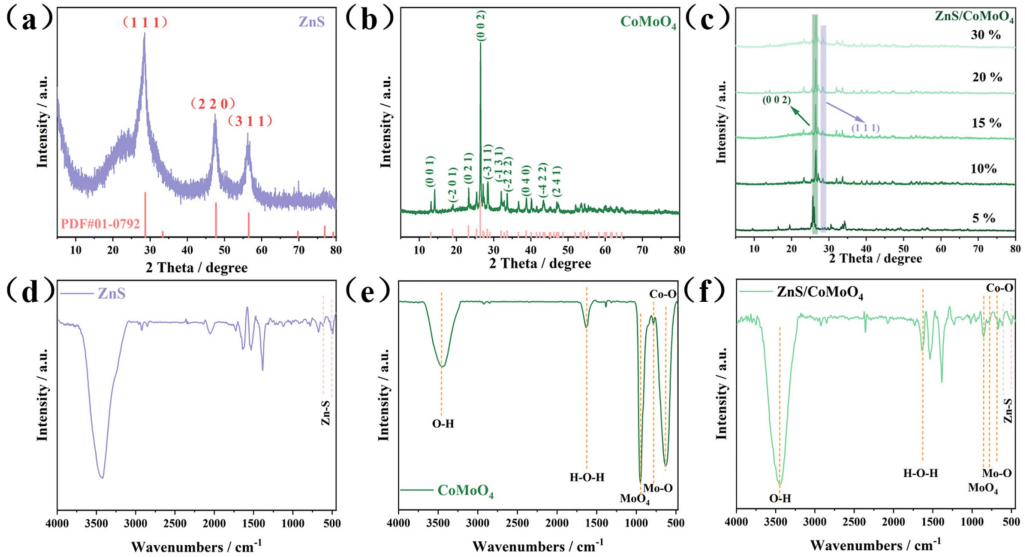


Figure 1. XRD patterns of (**a**) ZnS, (**b**) $CoMoO_4$, and (**c**) ZnS/$CoMoO_4$ composites; FT-IR spectra of (**d**) ZnS, (**e**) $CoMoO_4$, and (**f**) ZnS/$CoMoO_4$ composites.

FT-IR spectroscopy was employed to probe the surface functional groups and chemical bonds (Figure 1d–f). In the spectrum of pristine ZnS (Figure 1d), the absorption band in the 600–800 cm^{-1} fingerprint region is ascribed to Zn–S stretching vibrations [23], while the broad band around 3400 cm^{-1} arises from O–H stretching of adsorbed water. For pristine $CoMoO_4$ (Figure 1e), the broad band at ~3420 cm^{-1} and the band at ~1620 cm^{-1} correspond to O–H stretching and H–O–H bending of adsorbed water molecules, respectively; the strong absorption at ~930 cm^{-1} is characteristic of Mo–O stretching in the MoO_4 tetrahedra, and the multiple bands between 600 and 800 cm^{-1} originate from Co–O stretching vibrations, collectively confirming the formation of the metal–oxygen framework of $CoMoO_4$ [15,16,26]. The spectrum of the composite (Figure 1f) retains all the O–H, H–O–H, Mo–O, and m signatures of $CoMoO_4$ while exhibiting the Zn–S absorption in the fingerprint region, corroborating the coexistence of the two phases. Compared with pristine $CoMoO_4$, no characteristic bands disappear, and only minor line-shape changes occur, implying that the hydrothermal coupling process leaves the $CoMoO_4$ framework intact. The persistence of the O–H bands points to surface hydroxyl groups, which can serve as active sites for ROS generation during photocatalysis [5,13].

Raman spectra of pristine $CoMoO_4$ and ZnS/$CoMoO_4$ are provided in Figures S1 and S2. The bands at 1357 and 1593 cm^{-1} are assigned to carbonate species formed by adsorption of atmospheric CO_2 onto surface basic sites, and the weak band at 1274 cm^{-1} is associated with S–O stretching of trace sulfate residues from the precursor, since no organic carbon source was involved in the synthesis. The higher-order signals at 1838 and 1929 cm^{-1} arise from multi-phonon coupling, combination, and overtone scattering between the intrinsic optical phonons of the ZnS and $CoMoO_4$ lattices; such satellite vibrations are characteristic of the composite heterostructure rather than of any impurity phase, in line with the XRD results.

X-ray photoelectron spectroscopy was used to examine the surface elemental composition, chemical states, and interfacial electronic interactions of the samples; all spectra were charge-corrected to the C 1s signal at 284.8 eV. The survey spectra (Figure 2) show only Zn and S signals for pristine ZnS and only Co, Mo, and O signals for pristine $CoMoO_4$, whereas the composite presents all five expected elements (Zn, S, Co, Mo, and O), preliminarily confirming successful coupling of the two components.

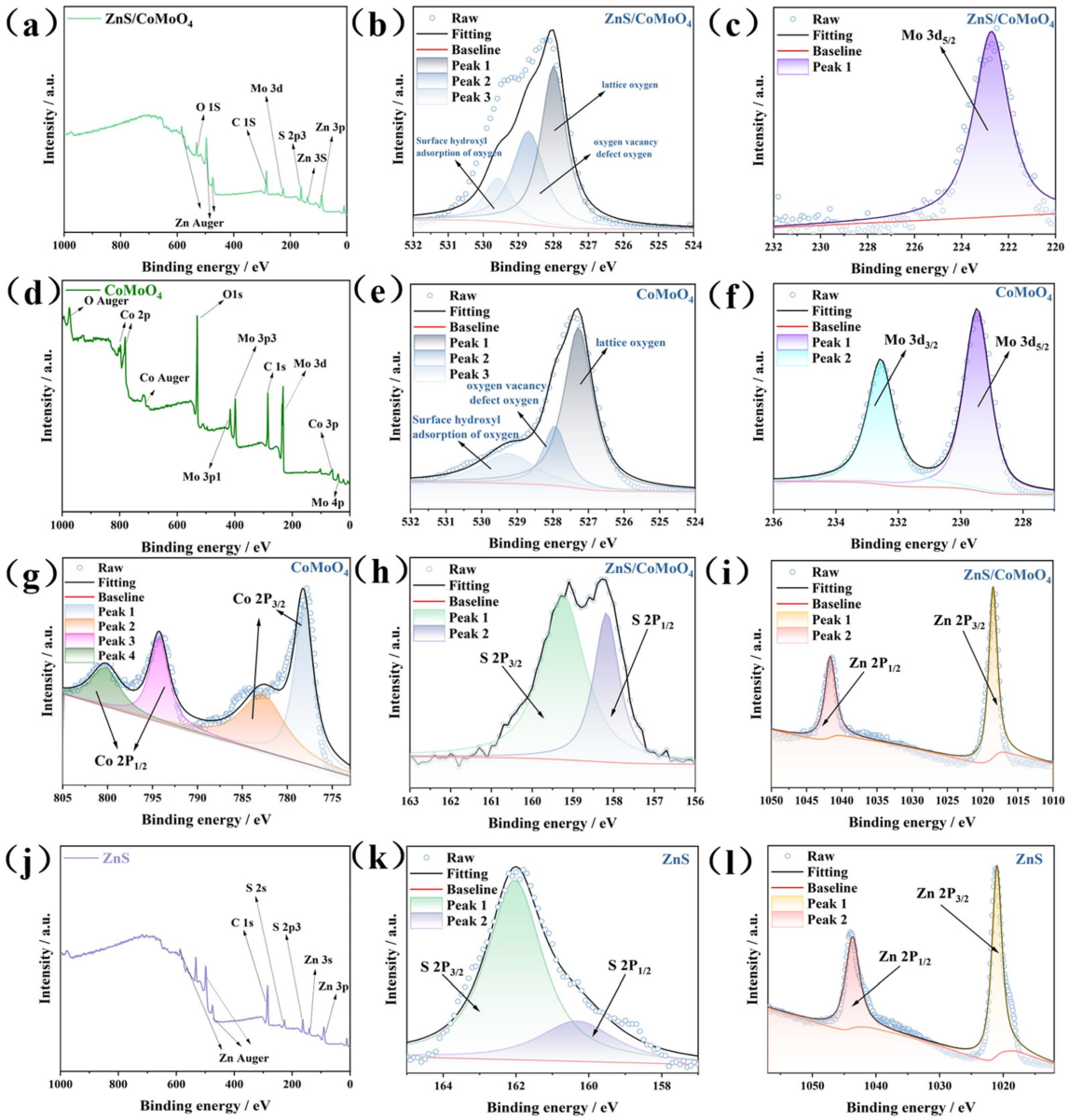


Figure 2. XPS survey spectra of $ZnS/CoMoO_4$ composites (**a**), $CoMoO_4$ (**d**), and ZnS (**j**); high-resolution XPS spectra of O (**b**,**e**), Mo 3d (**c**,**f**), Co 2p (**g**), S 2p (**h**,**k**), and Zn 2p (**i**,**l**) of the materials.

The high-resolution O 1s spectra reveal notable defect evolution upon coupling. For pristine $CoMoO_4$ (Figure 2e), the O 1s envelope deconvolutes into lattice oxygen at 527.4 eV (58.2% of the total area), oxygen-vacancy-related oxygen at 528.0 eV (16.5%), and surface hydroxyl/adsorbed-water oxygen at 529.3 eV. For the $ZnS/CoMoO_4$ composite (Figure 2b), the lattice-oxygen component red-shifts slightly to 527.9 eV, and its share drops to 42.7%, while the oxygen-vacancy component shifts to 528.8 eV and expands to 29.6%—an increase of 13.1 percentage points relative to the pristine sample. Evidently, interfacial coupling with ZnS perturbs the ordered metal–oxygen network of $CoMoO_4$ and generates abundant oxygen vacancies. Oxygen vacancies are well documented to act as electron-trapping centers that suppress carrier recombination and provide highly active catalytic sites [33].

The Mo 3d spectra furnish evidence of interfacial charge redistribution. Pristine $CoMoO_4$ (Figure 2f) displays a typical spin–orbit doublet with Mo 3d5/2 at 229.5 eV and Mo 3d3/2 at 232.8 eV, characteristic of Mo^{6+} [15,26]. In the composite (Figure 2c), the Mo 3d5/2 component shifts to 229.2 eV ($\Delta = -0.3$ eV) and Mo 3d3/2 to 232.5 eV, with a slightly broadened full width at half maximum and reduced symmetry, signaling an increased

electron density around Mo atoms—i.e., electron accumulation on the $CoMoO_4$ side. Conversely, for pristine ZnS, the S 2p doublet at 160.5 and 162.2 eV and the Zn 2p signal both correspond to the standard Zn^{2+}/S^{2-} valence states (Figure 2h,i,k,l); after coupling, the Zn 2p and S 2p peaks of the composite shift to higher binding energy by 0.3 eV, indicating electron depletion on the ZnS side. The opposing shift directions of the Mo 3d versus Zn 2p/S 2p signals collectively indicate that an intimate heterojunction—rather than a simple physical mixture—was constructed and that a directed electron-transfer channel from ZnS to $CoMoO_4$ is established at the interface under equilibrium, consistent with Fermi-level equilibration between the two semiconductors [20,21,30]. It should be emphasized that these ex situ shifts establish the intimate contact and the direction of the built-in field—a necessary condition for the S-scheme configuration—but by themselves do not distinguish it from a type-II pathway; the full mechanistic assignment is discussed in Section 2.5 based on the complete evidence set. In combination with the profuse oxygen vacancies, this directed interfacial charge redistribution promotes the separation and migration of photogenerated carriers and reduces electron–hole recombination, accounting at the electronic-structure level for the superior photocatalytic behavior of the composites.

2.2. Morphological Structure

The morphology of the samples was inspected by FE-SEM (Figure 3a–i). Pristine $CoMoO_4$ consists of one-dimensional nanorods several micrometers in length and ~100 nm in diameter that stack into a loose network, with relatively smooth rod surfaces (Figure 3a–c). Pristine ZnS appears as well-dispersed, uniform microspheres 1–2 μm in diameter with smooth surfaces (Figure 3d–f), a morphology typical of thiourea-mediated hydrothermal sulfides [9]. In the composite (Figure 3g–i), ZnS microspheres and $CoMoO_4$ nanorods coexist, with the $CoMoO_4$ nanorods anchored on the microsphere surfaces; at high magnification, the sphere surfaces become rougher, evidencing intimate interfacial contact between the two phases. This orientation is corroborated by the TEM-EDS maps (Figure 4a), in which Zn and S concentrate in the microsphere regions while Co, Mo, and O are distributed over the same and adjacent regions, and it follows naturally from the growth sequence: homogeneous nucleation of ZnS microspheres (1–2 μm) in the presence of the pre-formed nanorods embeds the rods at the sphere surfaces. Such tight junctions provide continuous pathways for the rapid migration and separation of photogenerated carriers across the interface, which is beneficial for photocatalysis [17,18].

The N_2 adsorption–desorption isotherms of the three samples (Figure 3j–l) are all of type IV with distinct H3-type hysteresis loops at high relative pressure (P/P_0 = 0.8–1.0), indicating mesoporous textures arising mainly from interparticle stacking [34]: the mesopores of $CoMoO_4$ originate from the packing of nanorods, and those of ZnS from the accumulation of microspheres. The textural parameters derived from these isotherms—the Brunauer–Emmett–Teller surface area (SBET), total pore volume, and average pore diameter—are summarized in Table S1. The composite exhibits a lower SBET and pore volume than either parent for two reasons: approximately 85 wt% of its mass is ZnS, the component with the lower specific surface area, so mass-weighted dilution alone pulls the composite value toward that of ZnS; in addition, the in situ growth of ZnS microspheres in the presence of the nanorods fills part of the inter-rod void space and partially envelopes the rod surfaces, blocking the mesopore network that arises from rod packing. Notably, despite its lower surface area, the composite outperforms both parents by a factor of 1.5–2.6 in rate constant (Section 3.4), which rules out accessible surface area as the origin of the enhancement and points instead to the interfacial electronic effect discussed in Section 2.5. The retained mesoporous channels still facilitate mass transport of pollutant molecules and expose accessible active sites, favoring the photocatalytic degradation reaction.

The TEM bright-field image, STEM image, and corresponding EDS elemental maps of the composite are displayed in Figure 4a. The contours of the Zn, S, O, Co, and Mo distributions coincide closely with the sample silhouette in the STEM image: Zn and S are homogeneously concentrated in the microsphere region (the ZnS component), while O, Co, and Mo are also well dispersed over the same region, indicating intimate contact between the two phases. The spatial overlap of all elements without noticeable aggregation or phase segregation directly confirms tight coupling of ZnS and $CoMoO_4$ and the successful construction of the heterojunction; the uniform interfacial contact provides continuous transport channels for photogenerated carriers and contributes to the improved photocatalytic performance.

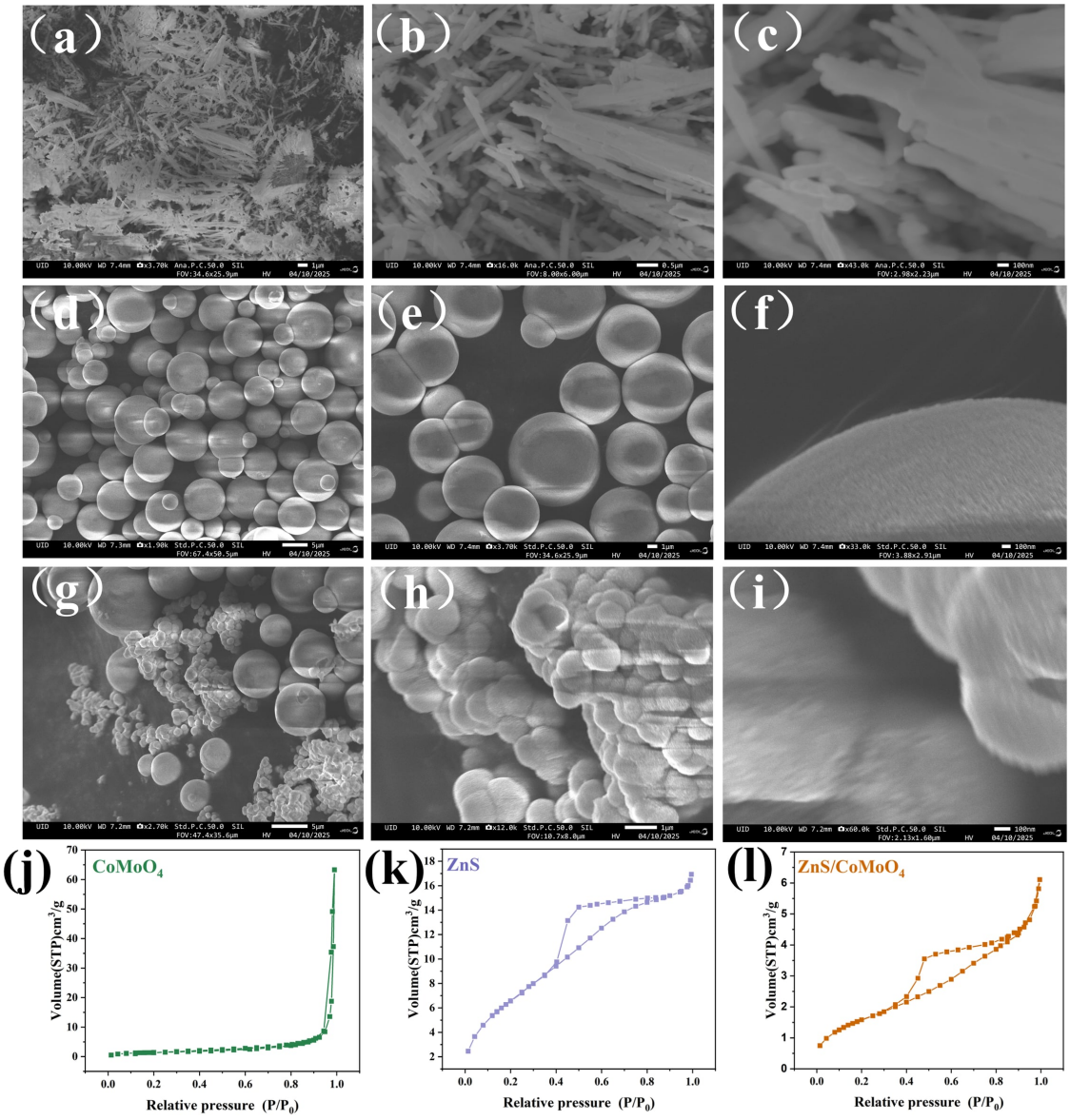


Figure 3. SEM images of (**a**–**c**) $CoMoO_4$, (**d**–**f**) ZnS, and (**g**–**i**) ZnS/$CoMoO_4$ composites; (**j**–**l**) N2 adsorption–desorption isotherms of the samples.

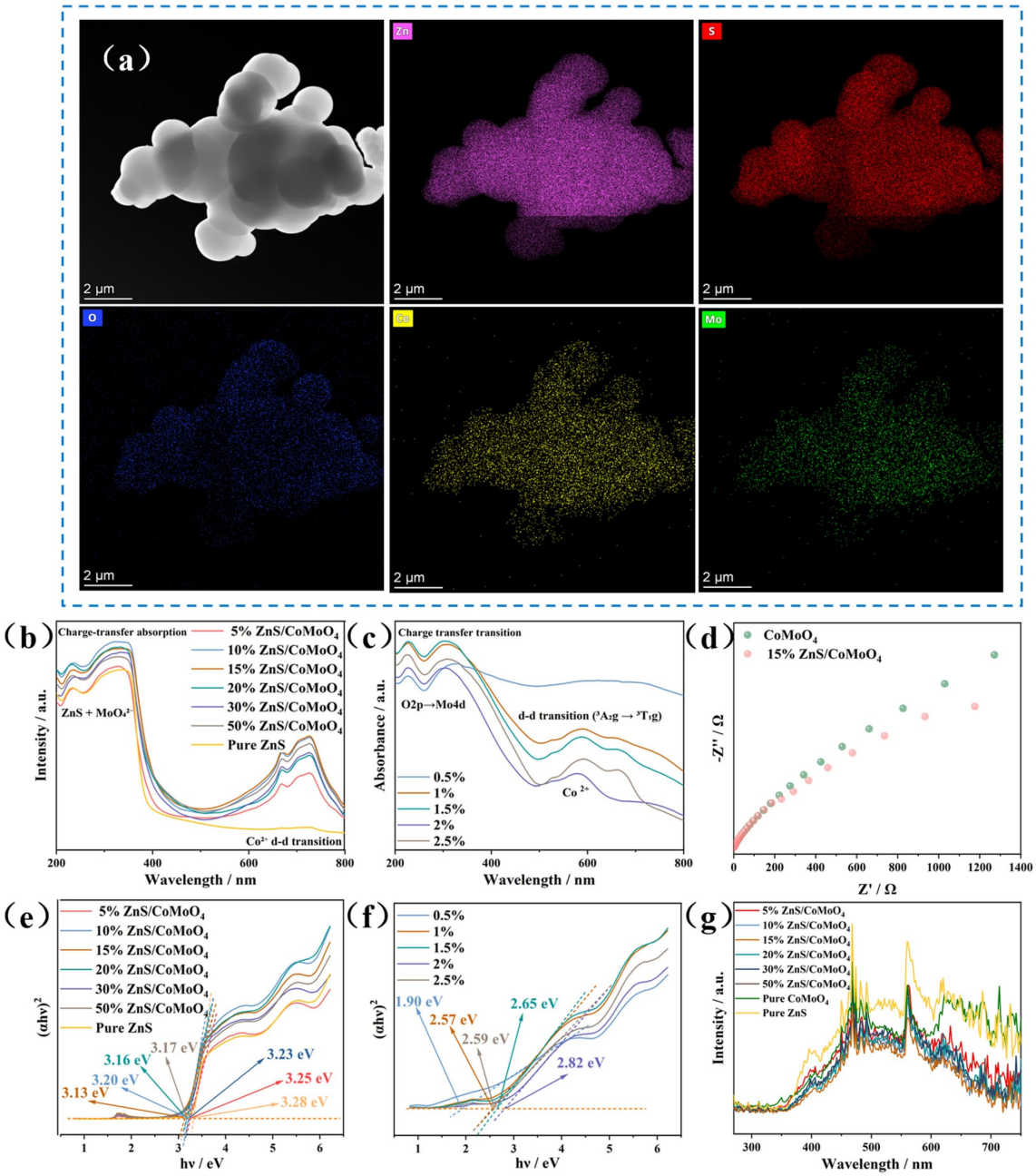


Figure 4. (**a**) EDS mapping of ZnS/$CoMoO_4$ composites; (**b**,**c**) UV–vis DRS and (**e**,**f**) the bandgap values of materials estimated by a related curve of $(\alpha h\nu)^2$ vs. photon energy plotted; (**d**) EIS responses of samples dropped onto a FTO electrode in the dark (0.1 M Na_2SO_4 solution); (**g**) photoluminescence spectra of the samples.

2.3. Optical Properties and Band Structure

UV–vis diffuse-reflectance spectroscopy was used to examine the light-harvesting capability and band structure of the composites (Figure 4b,c,e,f). Pristine ZnS absorbs strongly only in the ultraviolet region, consistent with its wide band gap [9,10]. After the introduction of $CoMoO_4$, the composites exhibit obvious absorption in the visible region, which is assigned to the d–d transitions of Co^{2+} and to O 2p → Mo 4d charge-transfer transitions of the molybdate [15,16,26]; among the series, the 15 wt% ZnS/$CoMoO_4$ sample shows the strongest visible-light capture. Apparent optical band gaps were extracted from Tauc plots of $(\alpha h\nu)^2$ versus photon energy [35]; pristine ZnS has a band gap of ~3.28 eV, and the heterojunctions display apparent gaps of 3.13–3.25 eV. For a two-phase

composite, this extrapolated value should be read as an apparent quantity describing the composite absorption edge rather than the band structure of a new chemical phase. The Tauc extrapolation is dominated by the strongest and steepest absorption edge—that of ZnS—while the weaker $CoMoO_4$ absorption (the d–d transitions of Co^{2+} and the O 2p → Mo 4d charge-transfer band) contributes a slowly varying absorption tail below the ZnS edge, so the intercept falls slightly below the ZnS value and depends on the loading-dependent weight of the molybdate contribution. Two observations support this superposition interpretation: the $CoMoO_4$ reflections remain at unshifted positions across the whole loading series (Figure 1c), arguing against substitutional doping or any significant modification of the bulk lattice, and the apparent gaps of the composites vary by only 0.12 eV over the 5–50 wt% series while always lying between the gaps of the two parents. The slightly broadened photoresponse nonetheless lowers the photon energy required for excitation and, together with the visible-light absorption of the molybdate component, constitutes the optical foundation for the enhanced photocatalytic activity.

Electrochemical impedance spectroscopy (EIS) was performed to evaluate interfacial charge transport (Figure 4d); in Nyquist plots, a smaller arc radius corresponds to a lower charge-transfer resistance. The arc radius of the 15 wt% ZnS/$CoMoO_4$ composite is markedly smaller than that of pristine $CoMoO_4$, testifying that heterojunction formation lowers the interfacial charge-transfer resistance and opens fast transport channels that suppress electron–hole recombination [17,24].

Photoluminescence (PL) spectroscopy probes the radiative recombination of photogenerated carriers; weaker emission indicates more efficient separation. As shown in Figure 4g, pristine ZnS exhibits the strongest PL intensity, revealing severe carrier recombination, while pristine $CoMoO_4$ shows a reduced intensity. All ZnS/$CoMoO_4$ heterojunction samples display clearly quenched emission, confirming that the heterointerface effectively promotes carrier migration and suppresses radiative recombination [24,25]. As the ZnS fraction increases from 5% to 50%, the PL intensity first decreases and then rises, because excessive ZnS induces particle agglomeration and introduces additional recombination centers. The 15 wt% sample shows the weakest PL signal—i.e., the highest charge-separation efficiency—demonstrating that an appropriate composite ratio maximizes the suppression of carrier recombination.

2.4. Photocatalytic Degradation of Methylene Blue

The visible-light photocatalytic performance of the series was evaluated using MB as the model pollutant (Figure 5a,b). In the first 30 min of dark stirring, the C/C_0 of MB decreased slightly for every sample and then plateaued, indicating that adsorption–desorption equilibrium was reached before irradiation [36]. After the lamp was switched on, the pollutant concentration decayed continuously. Within 120 min of visible-light irradiation (150 min total including the adsorption stage), pristine ZnS degraded only 43.2% of MB and pristine $CoMoO_4$ 65.4%, whereas all heterojunction samples performed markedly better: 72.7% and 81.2% for the 5 wt% and 10 wt% composites, a maximum of 88.8% for the 15 wt% composite, and 84.7%, 79.1%, and 71.5% for the 20 wt%, 30 wt%, and 50 wt% samples, respectively. The activity thus follows a volcano-type dependence on the ZnS loading fraction. The evolution of the full UV–vis absorption spectrum during irradiation is shown in Figure 5c. With increasing illumination time, the 664 nm band decays progressively without the appearance of new bands in the visible region, consistent with the destruction of the thiazine chromophore and successive N-demethylation rather than mere dilution. The degradation performance of the 15 wt% ZnS/$CoMoO_4$ composite is compared with representative ZnS- and $CoMoO_4$-based photocatalysts [37–39] in Table S2 (Supporting Information). Under comparable visible-light conditions, the composite lies

in the upper-middle range of the reported systems while requiring the lowest catalyst loading of the comparison and a single-step hydrothermal synthesis without calcination or activation steps.

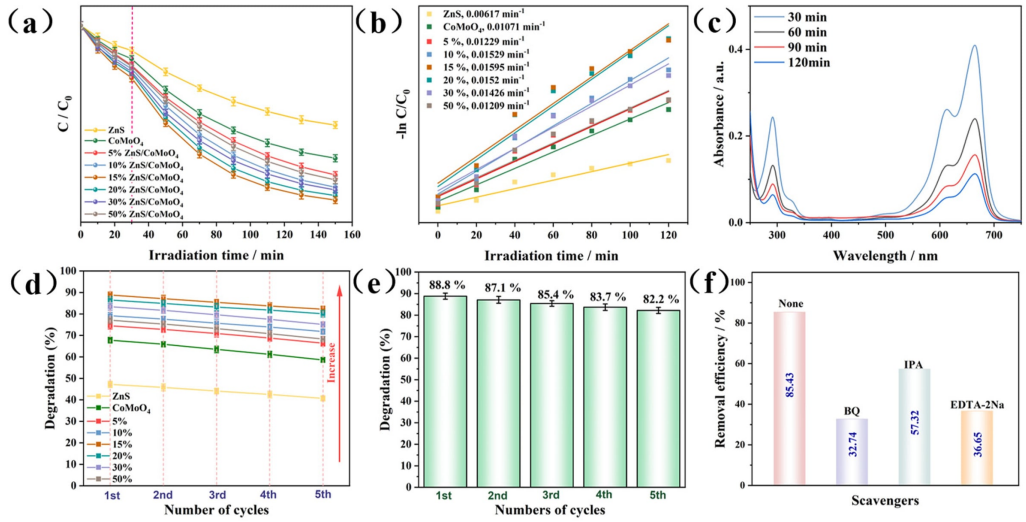


Figure 5. (**a**) Visible-light-driven photocatalytic activities and (**b**) their kinetic constants of ZnS/$CoMoO_4$ composites in the degradation of MB. (**c**) Photocatalytic degradation of 15% ZnS/$CoMoO_4$ and (**d**,**e**) cycling runs in the photodegradation of MB by ZnS/$CoMoO_4$ composites. (**f**) Photodegradation of MB with various scavengers.

To quantify the reaction kinetics, the irradiation-stage data were fitted to the pseudo-first-order Langmuir–Hinshelwood model, $\ln(C_0/C) = kt$ [36]. The fitted rate constants k are 0.00617 and 0.01071 min^{-1} for pristine ZnS and $CoMoO_4$, and 0.01229, 0.01529, 0.01595, 0.01520, 0.01426, and 0.01209 min^{-1} for the 5, 10, 15, 20, 30, and 50 wt% composites, respectively. The 15 wt% sample possesses the largest k, 2.58 and 1.49 times those of pristine ZnS and $CoMoO_4$; the 20 wt% sample follows closely, and all data points fit the linear model well, confirming that the degradation obeys pseudo-first-order kinetics. An appropriate ZnS loading builds an intimate heterojunction interface that promotes charge separation, whereas excessive ZnS causes severe agglomeration that shields surface active sites and introduces interfacial defects that accelerate recombination, causing the activity to decay.

To identify the dominant reactive species, radical-scavenging experiments were carried out under identical conditions by adding p-benzoquinone (BQ, 1 mM, an $\bullet O_2^-$ scavenger), EDTA-2Na (5 mM, a hole scavenger), and isopropanol (IPA, 10 mM, a •OH scavenger) to the reaction system (Figure 5f). The degradation efficiency of MB over the 15 wt% ZnS/$CoMoO_4$ composite decreased from 88.8% to 32.7% with BQ, 36.6% with EDTA-2Na, and 57.3% with IPA within 120 min. The strongest suppression by BQ and EDTA-2Na identifies $\bullet O_2^-$ and photogenerated holes as the principal reactive species, while the moderate effect of IPA assigns •OH a secondary role. This order is precisely what the S-scheme charge transfer predicts: the electrons retained in the ZnS conduction band (ECB = −1.10 V vs. NHE) readily reduce dissolved O_2 to $\bullet O_2^-$, and the holes retained in the $CoMoO_4$ valence band (EVB = +2.45 V vs. NHE) oxidize surface hydroxyls and water to •OH (Figure 6), so both radical generation channels of the S-scheme junction are confirmed by the scavenging results.

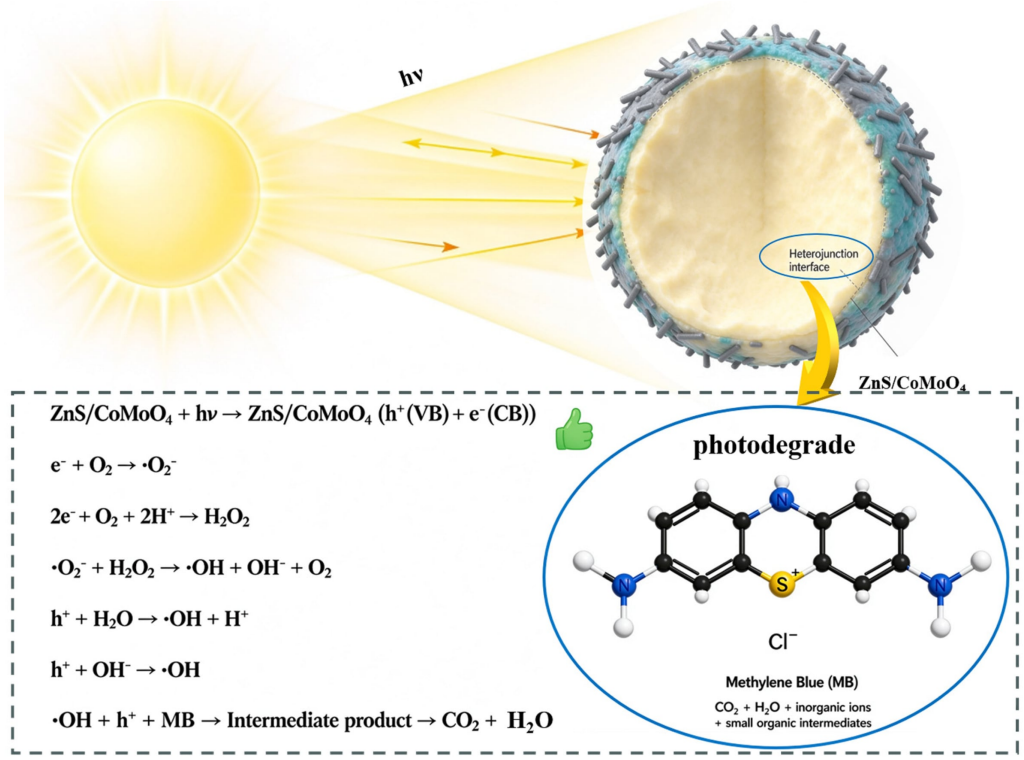


Figure 6. Schematic diagram of photocatalytic effect enhancement.

Reusability is a key criterion for practical application. As shown in Figure 5d,e, after five consecutive cycles, the degradation efficiency of pristine ZnS fell from 47.2% to 40.8% and that of pristine $CoMoO_4$ from 67.8% to 58.5%, whereas the heterojunction samples deactivated more gently. The 15 wt% ZnS/$CoMoO_4$ composite maintained the best performance throughout, retaining 82.2% efficiency after five cycles (88.8%, 87.1%, 85.4%, 83.7%, and 82.2% in cycles 1–5) with a total activity loss of only ~6.6%, confirming its excellent cycle stability; the other composites likewise retained the major part of their initial activity. The gentler deactivation of the heterojunctions indicates that the intimate interface mitigates the photocorrosion of ZnS [8,11,40]. Within the mechanistic framework discussed in Section 2.5, this observation also carries diagnostic weight: under a type-II alignment, the photogenerated holes would accumulate in the valence band of ZnS (EVB ≈ +2.2 V vs. NHE), which is thermodynamically capable of oxidizing sulfide to elemental sulfur, so photocorrosion would be expected to accelerate, not attenuate, upon coupling; the observed stabilization is instead what the S-scheme picture predicts, because the interfacial recombination step removes holes from the ZnS valence band. XRD patterns of the composite before and after reaction (Figure S3) show the CoMoO4 (002), (−131), and (−222) reflections together with the ZnS (111) and (220) reflections at unshifted positions and without new impurity peaks, demonstrating that the phase composition and crystal structure are essentially preserved during photodegradation; the slight decline of peak intensity after cycling may stem from mild surface etching or partial aggregation during prolonged irradiation. XRD patterns of the composite before and after reaction (Figure S3) show the $CoMoO_4$ (002), (−131), and (−222) reflections together with the ZnS (111) and (220) reflections at unshifted positions and without new impurity peaks, demonstrating that the phase composition and crystal structure are essentially preserved during photodegradation; the slight decline of peak intensity after cycling may stem from mild surface etching or partial aggregation during prolonged irradiation.

2.5. Mechanism Study of Activity Enhancement of ZnS/$CoMoO_4$

The PL emission of all composites is quenched relative to both parent semiconductors, reaching the lowest intensity at a ZnS loading of 15 wt% (Figure 4g), which demonstrates that non-radiative interfacial charge transfer proceeds most efficiently at this optimal composition. In line with this observation, the EIS arc radius of the 15 wt% composite is substantially smaller than that of pristine $CoMoO_4$ (Figure 4d), indicating reduced interfacial charge-transfer resistance. Meanwhile, the oxygen-vacancy contribution to the O 1s spectrum increases from 16.5% for pristine $CoMoO_4$ to 29.6% for the composite, introducing extra trap sites to facilitate charge separation. Cyclic stability tests reveal that the 15 wt% composite retains favorable reusability, with only a 7.4% drop in its initial degradation activity over five cycles, compared with activity losses of 13.6% for pristine ZnS and 13.7% for pristine $CoMoO_4$ under identical conditions; post-cycling XRD characterization (Figure S3) confirms the absence of new crystalline phases or peak shifts. Based on the collective evidence above, an S-scheme charge-transfer mechanism is proposed for the photodegradation of MB over ZnS/$CoMoO_4$ (Figure 6) [20,21,30]. Under visible-light irradiation, both ZnS microspheres and $CoMoO_4$ nanorods are photoexcited, promoting valence-band electrons to the conduction band and generating electron–hole pairs. Because the two phases are in intimate contact, a built-in electric field forms at the interface; driven by this field, the photogenerated electrons in the $CoMoO_4$ conduction band recombine with the holes in the ZnS valence band at the interface, consuming the charge carriers with weaker redox power. The electrons accumulated in the ZnS conduction band (strong reduction ability) and the holes retained in the $CoMoO_4$ valence band (strong oxidation ability) are thus preserved.

Figure 7 summarizes the band alignment quantitatively. ZnS possesses a band gap of 3.28 eV (Tauc plot, Figure 5e); adopting the conduction-band position of sphalerite ZnS reported in the literature (E_{CB} = −1.10 V vs. NHE), its valence band lies at +2.18 V. $CoMoO_4$ exhibits Eg = 2.82 eV (Tauc plot of the 2:1 sample, Figure 4f); with E_{CB} = −0.35 V vs. NHE taken from the literature, its valence band is located at +2.47 V. The two band structures are therefore staggered, with ZnS acting as the reduction side and $CoMoO_4$ as the oxidation side—precisely the geometry required for an S-scheme junction. Upon contact, the Fermi-level equilibration observed by XPS establishes a built-in electric field directed from ZnS to $CoMoO_4$, under which the photogenerated electrons in the $CoMoO_4$ conduction band recombine with the holes in the ZnS valence band at the interface. The carriers that survive this recombination are thermodynamically competent for ROS generation: the electrons accumulated in the ZnS conduction band (−1.10 V) lie well above the $O_2/{\bullet}O_2^-$ potential (−0.33 V vs. NHE) and readily reduce dissolved O_2 to ${\bullet}O_2^-$, while the holes retained in the $CoMoO_4$ valence band (+2.47 V) lie below the ${\bullet}OH/OH^-$ potential (+1.99 V vs. NHE) and oxidize surface hydroxyls and water to ●OH. This quantitative band picture is consistent with the enhanced charge separation evidenced by the PL quenching of the composites and the smaller EIS arc radius of the 15 wt% composite (Figure 4d,g). The ZnS conduction-band electrons reduce dissolved O_2 to ${\bullet}O_2^-$ radicals, while the $CoMoO_4$ valence-band holes oxidize surface-adsorbed water/hydroxyl groups into ●OH radicals [5,36]. Together with the residual holes, ${\bullet}O_2^-$ and ●OH attack MB molecules, progressively cleaving the aromatic rings and mineralizing the dye into CO_2, H_2O, and small inorganic species [36]. By eliminating the useless carriers while retaining the useful ones, the S-scheme junction effectively suppresses bulk recombination and endows ZnS/$CoMoO_4$ with visible-light photocatalytic activity superior to that of either bare semiconductor.

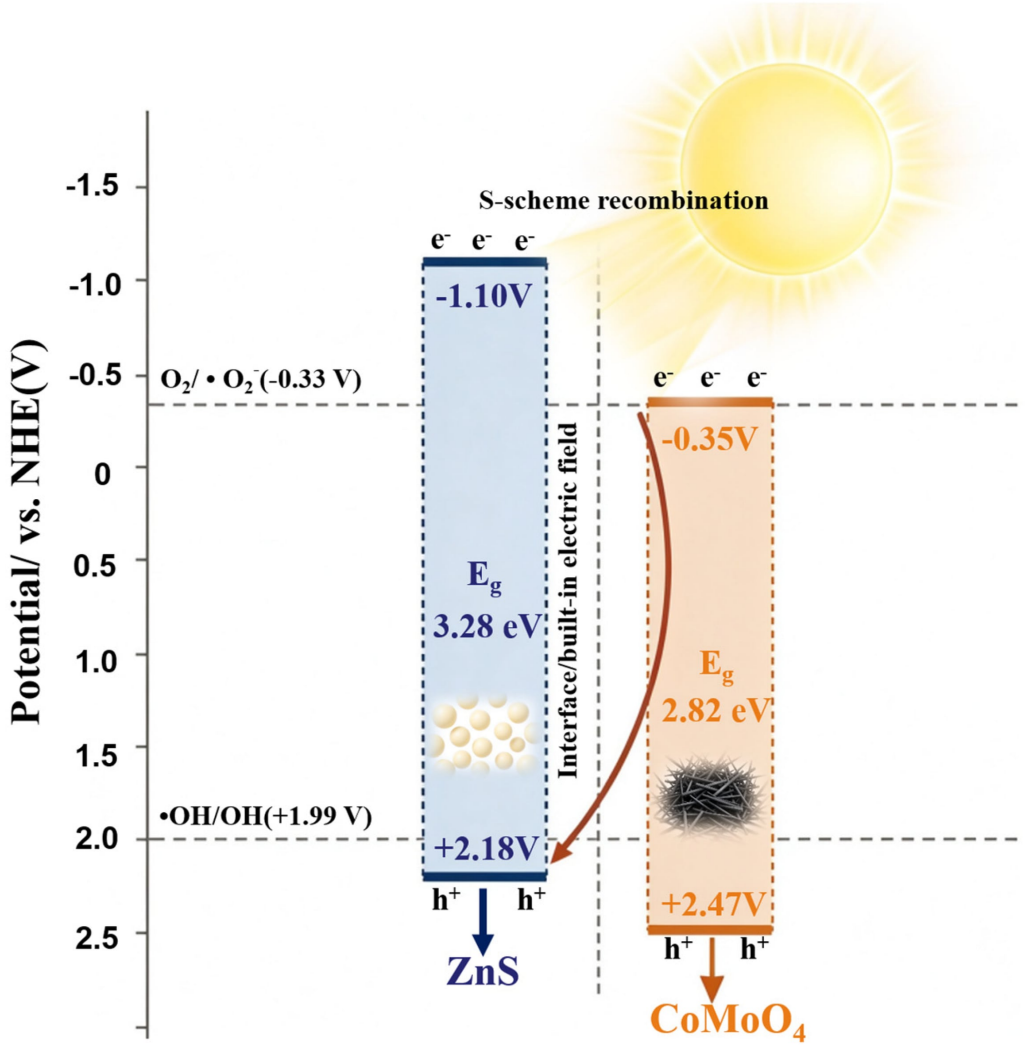


Figure 7. Schematic illustration of the band alignment and S-scheme charge-transfer pathway over the ZnS/CoMoO4 heterojunction after contact under visible-light irradiation.

3. Experiment

All chemical reagents used in this experiment were of analytical grade and used as received without further purification. Laboratory self-made deionized water was used throughout the experiment. Zinc acetate, thiourea, sodium molybdate dihydrate, and cobalt nitrate hexahydrate were employed as synthetic precursors, and anhydrous ethanol was used for washing the hydrothermal products. Photocatalytic degradation of methylene blue (MB) was used to evaluate the photocatalytic activity of ZnS/$CoMoO_4$ composites under visible-light irradiation (400–780 nm). A xenon lamp system (CEL-HXF 300, Ceavlight, Beijing, China) served as the light source, and the light power density at the reactor position was calibrated to be 7.5 mW/cm^2. In a typical photocatalytic test, 40 mg of catalyst powder was dispersed into 40 mL of MB aqueous solution with an initial concentration of 10 mg/L. Before light irradiation, the suspension was magnetically stirred in the dark for 30 min to reach adsorption–desorption equilibrium. During the photodegradation process, 5 mL aliquots were collected at 30 min intervals. After centrifugation to separate solid catalyst particles, the absorbance of the supernatant was measured at 664 nm using a UV–vis spectrophotometer. All photocatalytic experiments in this work were performed under identical operational conditions to enable a reliable comparison among samples with different ZnS loading contents. The details are shown in the Supporting Information.

3.1. Preparation of ZnS

Pure ZnS nanomaterials were synthesized via a hydrothermal method. Briefly, 5.571 g zinc acetate and 2.971 g thiourea were dissolved in 30 mL deionized water. The charges correspond to 5.571 g $Zn(CH_3COO)_2{\cdot}2H_2O$ (0.0254 mol) and 2.971 g thiourea (0.0390 mol), i.e., the zinc–thiourea molar ratio was 1:1.54. The moderate thiourea excess was adopted deliberately. Thiourea decomposes only gradually under hydrothermal conditions and thus serves as a buffered sulfur source as well as a structure-directing agent, and this ratio reproducibly yielded uniform ZnS microspheres in our preliminary runs. The mixed solution was magnetically stirred for 1 h and then ultrasonicated for another 1 h to obtain a homogeneous precursor suspension. The suspension was transferred into a 50 mL stainless steel autoclave with a polytetrafluoroethylene (PTFE) liner and maintained at 180 °C for 12 h. After the autoclave naturally cooled to room temperature, the precipitate was collected by centrifugation. The solid product was washed repeatedly with deionized water and anhydrous ethanol alternately and dried in an oven at 60 °C for 12 h to obtain pure ZnS powder.

3.2. Preparation of $CoMoO_4$

$CoMoO_4$ materials were hydrothermally synthesized with the molar ratio of cobalt nitrate hexahydrate to sodium molybdate dihydrate varying from 0.5:1 to 1:1, 1.5:1, 2:1, and 2.5:1. This series was used to screen the Co/Mo stoichiometry, which controls both the phase purity and the morphology of the hydrothermal product: cobalt-rich charges favor the growth of phase-pure monoclinic $CoMoO_4$ nanorods, whereas molybdate-rich charges leave amorphous molybdate residues and give irregular aggregates. The 2:1 charge (1.413 g $Co(NO_3)_2{\cdot}6H_2O$, 4.855 mmol; 0.581 g $Na_2MoO_4{\cdot}2H_2O$, 2.401 mmol) yielded phase-pure monoclinic $CoMoO_4$ (Figure 2b) with the most uniform nanorod morphology and was therefore selected as the matrix for all composite experiments; it is taken as an example below. First, 1.413 g cobalt nitrate hexahydrate and 0.581 g sodium molybdate dihydrate were separately dissolved in 10 mL deionized water. The two solutions were mixed and magnetically stirred for 30 min to ensure sufficient mixing. Subsequently, the mixed solution was transferred into a 50 mL PTFE-lined stainless steel autoclave and reacted at 120 °C for 12 h. After the reaction, the autoclave was cooled to room temperature. The precipitate was centrifuged and washed 5–6 times with deionized water to remove by-products and unreacted raw materials. The washed sample was dried in an oven at 60 °C. Afterwards, the dried powder was placed in a crucible and calcined at 480 °C for 2 h. Finally, the product was ground in an agate mortar to obtain $CoMoO_4$ nanomaterials.

3.3. Preparation of ZnS/$CoMoO_4$ Composites

A series of ZnS/$CoMoO_4$ nanocomposites with ZnS mass fractions of 5 wt%, 10 wt%, 15 wt%, 20 wt%, 30 wt%, and 50 wt% were prepared by a one-step hydrothermal method. The schematic diagram of the fabrication process is shown in Figure 8. Taking the sample with 15 wt% ZnS as an example, 5.572 g of zinc acetate, 2.974 g of thiourea, and 0.0583 g of pre-synthesized $CoMoO_4$ were dispersed in 30 mL of deionized water. The suspension was magnetically stirred for 1 h and ultrasonicated for another 1 h to achieve adequate dispersion and mixing. The suspension was then transferred into a 50 mL PTFE-lined autoclave and hydrothermally treated at 180 °C for 12 h. After the system naturally cooled to room temperature, the solid precipitate was harvested by centrifugation, washed several times with deionized water and anhydrous ethanol, and dried in an oven at 60 °C for 12 h to obtain composite powder. For the preparation of samples with other ZnS loadings, the feeding amounts of zinc acetate and thiourea remained unchanged; only the added mass of $CoMoO_4$ was adjusted, while all other experimental parameters were kept identical.

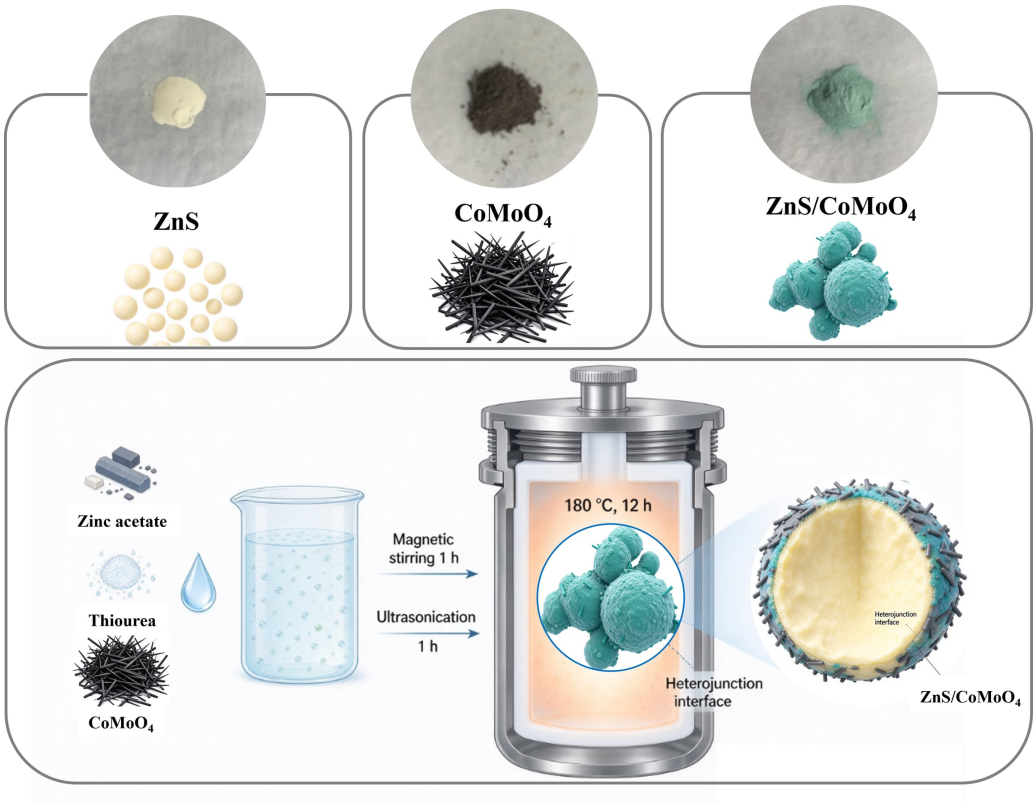


Figure 8. Schematic illustration of the fabrication of $ZnS/CoMoO_4$ nanocomposites.

3.4. Characterization and Photocatalytic Reaction

Multiple characterization techniques, including X-ray diffraction (XRD), Fourier-transform infrared spectroscopy (FT-IR), Raman spectroscopy, X-ray photoelectron spectroscopy (XPS), field-emission scanning electron microscopy (FE-SEM), nitrogen adsorption–desorption measurement, elemental mapping, transmission electron microscopy (TEM), ultraviolet–visible diffuse reflectance spectroscopy (UV-vis DRS), electrochemical impedance spectroscopy (EIS), and photoluminescence spectroscopy (PL), were employed to characterize the morphology and structure of the $ZnS/CoMoO_4$ nanocomposites. The photocatalytic performance of $ZnS/CoMoO_4$ was evaluated by the photodegradation of methylene blue (10 mg/L) under visible-light irradiation. Further details are provided in Supporting Information S1.

A 300 W xenon lamp equipped with a 420 nm cutoff filter was used to simulate visible light for the photocatalytic degradation experiment. In this test, 500 mL of methylene blue solution with a concentration of 10 mg/L was used as simulated wastewater, and 0.14 g of photocatalyst powder was added to the reaction system. Before turning on the light source, the suspension was stirred in the dark for 30 min to achieve adsorption–desorption equilibrium. During the photocatalytic reaction, 2 mL aliquots of the suspension were collected at scheduled time intervals. The samples were centrifuged at 10,000 r/min for 5 min, and the supernatant was collected for absorbance measurement at the characteristic wavelength of 664 nm using a UV–visible spectrophotometer (UV-1800).

XPS measurements were carried out on pristine ZnS, pristine $CoMoO_4$, and the optimal 15 wt% composite; the mechanistic quantity they address—the direction and magnitude of the interfacial charge redistribution—is defined by these three samples. As a photolysis control, an MB solution of the same concentration was irradiated for 120 min under identical conditions but without catalyst; the concentration decreased by only 4.5%, confirming that direct photolysis and lamp heating contribute negligibly to the degradation reported below.

The 420 nm cutoff filter removes the near-UV output of the lamp to which MB photolysis is most sensitive, and the reactor was thermostatted by recirculating cooling water. The corresponding catalyst loading is 1 g L^{-1}, and the natural pH of the suspension was ≈6.8; these operating parameters were kept fixed across the whole loading series so that the composition comparison remains internally consistent.

4. Conclusions

A series of ZnS/$CoMoO_4$ heterojunction nanocomposites with ZnS loadings of 5–50 wt% were successfully fabricated via a one-step hydrothermal method. XRD, FT-IR, and XPS analyses confirm the coexistence of the ZnS and $CoMoO_4$ phases and the formation of an intimate heterointerface rather than a physical mixture; coupling also refines the $CoMoO_4$ grains and multiplies surface oxygen vacancies, enriching the accessible active sites. The visible-light degradation of MB shows a volcano-type dependence on ZnS content, with all composites outperforming the bare semiconductors. The 15 wt% ZnS/$CoMoO_4$ composite exhibits the optimal activity—88.8% MB degradation within 120 min ($k = 0.01595\ min^{-1}$)—and preserves 82.2% efficiency after five cycles. Excessive ZnS loading causes agglomeration and introduces recombination centers, accounting for the activity decline at high loadings. The enhancement is consistent with the S-scheme band alignment at the heterointerface: the built-in electric field drives directional charge migration and separation, suppressing electron–hole recombination while retaining strongly reducing electrons and strongly oxidizing holes, and the quantified band alignment shows that the surviving carriers are thermodynamically competent for both $\bullet O_2^-$ and •OH generation. This work demonstrates that building semiconductor heterojunctions through a simple hydrothermal route is an effective strategy for strengthening the visible-light photocatalytic capability of molybdate–sulfide systems and provides a useful experimental basis for designing efficient heterojunction photocatalysts for organic dye wastewater treatment.

Supplementary Materials: The following supporting information can be downloaded at https://www.mdpi.com/article/10.3390/catal16111027/s1, Figure S1: Raman spectroscopy analysis of Pure $CoMoO_4$; Figure S2. Raman spectroscopy analysis of Pure ZnS/$CoMoO_4$; Figure S3. Comparison of XRD spectra before and after reaction. Table S1: Textural parameters of the samples derived from the N_2 physisorption isotherms; Table S2. Comparison of the photocatalytic degradation of MB over the present composite and reported photocatalysts. The information on activity characterization and parameter setting, as well as XRD spectra and Raman spectroscopy, is available in the online version.

Author Contributions: Conceptualization, T.D. and Z.W.; formal analysis, H.Z.; data curation, H.W. (Haiyang Wang); writing—original draft preparation, Y.Z.; writing—review and editing, S.Z.; visualization, Y.P., H.W. (Hairu Wang), S.D., and H.Q.; supervision, T.D.; project administration, T.D.; funding acquisition, T.D. All authors have read and agreed to the published version of the manuscript.

Funding: This work was supported by the Shaanxi Provincial Department of Education General Special Scientific Research Project [Grant No. 25JK0708]; the Open topic of key laboratory of Synthetic chemistry and application in Anhui Province [Grant No. APKLSCA202502]; the Xijing University High-Level Talent Fund Project [Grant No. XJ24B04]; and the Government-invested Geological Exploration Project of Shaanxi Province (Grant No. 61202615511, Task Book No. 2026-GY-021), funded by the Shaanxi Provincial Department of Natural Resources and the Shaanxi Provincial Department of Finance.

Data Availability Statement: No new data were generated or analyzed in support of this review. All data cited in this work are available from the corresponding original references.

Acknowledgments: The authors are grateful for the technical support received during the preparation of this review. During the preparation of this manuscript, the authors used DeepL for language polishing and sentence reorganization. The authors have reviewed and edited all outputs and take full

responsibility for the content of this publication. This work was partially supported by the Shaanxi Provincial Department of Education General Special Scientific Research Project (25JK0708); the Open topic of key laboratory of Synthetic chemistry and application in Anhui Province (APKLSCA202502); the Xijing University High-Level Talent Fund Project (XJ24B04); and The Government-invested Geological Exploration Project of Shaanxi Province (Grant No. 61202615511, Task Book No. 2026-GY-021), funded by the Shaanxi Provincial Department of Natural Resources and the Shaanxi Provincial Department of Finance.

Conflicts of Interest: The authors declare no conflicts of interest.

References

1. Kant, R. Textile dyeing industry an environmental hazard. *Nat. Sci.* **2012**, *4*, 22–26.
2. Holkar, C.R.; Jadhav, A.J.; Pinjari, D.V.; Mahamuni, N.M.; Pandit, A.B. A critical review on textile wastewater treatments: Possible approaches. *J. Environ. Manag.* **2016**, *182*, 351–366. [CrossRef]
3. Glazar, D.; Simončič, B. TiO_2 and ZnO as advanced photocatalysts for effective dye degradation in textile wastewater. *Tekstilec* **2023**, *66*, 178–198. [CrossRef]
4. Oturan, M.A.; Aaron, J.-J. Advanced oxidation processes in water/wastewater treatment: Principles and applications. A review. *Crit. Rev. Environ. Sci. Technol.* **2014**, *44*, 2577–2641. [CrossRef]
5. Hoffmann, M.R.; Martin, S.T.; Choi, W.; Bahnemann, D.W. Environmental applications of semiconductor photocatalysis. *Chem. Rev.* **1995**, *95*, 69–96. [CrossRef]
6. Fujishima, A.; Honda, K. Electrochemical photolysis of water at a semiconductor electrode. *Nature* **1972**, *238*, 37–38. [CrossRef]
7. Asahi, R.; Morikawa, T.; Ohwaki, T.; Aoki, K.; Taga, Y. Visible-light photocatalysis in nitrogen-doped titanium oxides. *Science* **2001**, *293*, 269–271. [CrossRef]
8. Isac, L.; Enesca, A. Recent developments in ZnS-based nanostructures photocatalysts for wastewater treatment. *Int. J. Mol. Sci.* **2022**, *23*, 15668. [CrossRef]
9. Fang, X.; Zhai, T.; Gautam, U.K.; Li, L.; Wu, L.; Bando, Y.; Golberg, D. ZnS nanostructures: From synthesis to applications. *Prog. Mater. Sci.* **2011**, *56*, 175–287. [CrossRef]
10. Zhang, Y.; Zhang, N.; Tang, Z.-R.; Xu, Y.-J. Graphene transforms wide band gap ZnS to a visible light photocatalyst. The new role of graphene as a macromolecular photosensitizer. *ACS Nano* **2012**, *6*, 9777–9789. [CrossRef]
11. Lee, S.L.; Chang, C.-J. Recent progress on metal sulfide composite nanomaterials for photocatalytic hydrogen production. *Catalysts* **2019**, *9*, 457. [CrossRef]
12. Sawant, D.P.; Kulkarni, S.B.; Dubal, D.P.; Lohar, G.M. Transition metal molybdates emerging materials for high-performance supercapacitors: A machine learning analysis. *Battery Energy* **2025**, *4*, e20240073. [CrossRef]
13. Chamani, S.; Sadeghi, E.; Unal, U.; Peighambardoust, N.S.; Aydemir, U. Tuning electrochemical hydrogen-evolution activity of $CoMoO_4$ through Zn incorporation. *Catalysts* **2023**, *13*, 798. [CrossRef]
14. Kumar, A.; Sharma, P.; Sharma, G.; Dhiman, P.; Shekh, M.; Sillanpää, M.; Stadler, F.J. Recent progress in advanced strategies to enhance the photocatalytic performance of metal molybdates for H_2 production and CO_2 reduction. *J. Alloys Compd.* **2024**, *971*, 172665. [CrossRef]
15. Pirhashemi, M.; Habibi-Yangjeh, A. Facile fabrication of novel ZnO/$CoMoO_4$ nanocomposites: Highly efficient visible-light-responsive photocatalysts in degradations of different contaminants. *J. Photochem. Photobiol. A Chem.* **2018**, *363*, 31–43. [CrossRef]
16. Aloui, T.; Fourati, N.; Khirouni, K.; Guermazi, S.; Guermazi, H.; Zerrouki, C. Green synthesis of β-$CoMoO_4$ nanowires catalyst for organic dye photodegradation. *Measurement* **2024**, *236*, 115171. [CrossRef]
17. Wang, H.; Zhang, L.; Chen, Z.; Hu, J.; Li, S.; Wang, Z.; Liu, J.; Wang, X. Semiconductor heterojunction photocatalysts: Design, construction, and photocatalytic performances. *Chem. Soc. Rev.* **2014**, *43*, 5234–5244. [CrossRef]
18. Low, J.; Yu, J.; Jaroniec, M.; Wageh, S.; Al-Ghamdi, A.A. Heterojunction photocatalysts. *Adv. Mater.* **2017**, *29*, 1601694. [CrossRef]
19. Tada, H.; Mitsui, T.; Kiyonaga, T.; Akita, T.; Tanaka, K. All-solid-state Z-scheme in CdS–Au–TiO_2 three-component nanojunction system. *Nat. Mater.* **2006**, *5*, 782–786. [CrossRef]
20. Xu, Q.; Zhang, L.; Cheng, B.; Fan, J.; Yu, J. S-scheme heterojunction photocatalyst. *Chem* **2020**, *6*, 1543–1559. [CrossRef]
21. Zhang, L.; Zhang, J.; Yu, H.; Yu, J. Emerging S-scheme photocatalyst. *Adv. Mater.* **2022**, *34*, 2107668. [CrossRef]
22. Manoj, G.M.; Shankar, H.; Patel, D.K.; Arumugam, N. Direct Z-scheme ZnS@g-C_3N_4 heterojunction photocatalysts synthesized via a single-step method for sunlight-assisted degradation of organic pollutants. *J. Water Process Eng.* **2025**, *79*, 108845. [CrossRef]
23. Santhi, K.; Harish, S.; Navaneethan, M.; Ponnusamy, S. Enhanced photocatalytic activities of TiO_2 through metal chalcogenides based nanocomposites (ZnS/TiO_2) for methylene blue degradation. *Surf. Interfaces* **2023**, *41*, 103205. [CrossRef]

24. Murillo-Sierra, J.C.; Hernández-Ramírez, A.; Zhao, Z.-Y.; Martínez-Hernández, A.; Gracia-Pinilla, M.A. Construction of direct Z-scheme WO_3/ZnS heterojunction to enhance the photocatalytic degradation of tetracycline antibiotic. *J. Environ. Chem. Eng.* **2021**, *9*, 105111. [CrossRef]
25. Murillo-Sierra, J.C.; Maya-Treviño, M.D.L.; Nuñez-Salas, R.E.; Pino-Sandoval, D.A.; Hernández-Ramírez, A. Facile synthesis of ZnS/WO_3 coupled photocatalyst and its application on sulfamethoxazole degradation. *Ceram. Int.* **2022**, *48*, 13761–13769. [CrossRef]
26. Zhang, X.; Lou, S.; Zeng, Y. Facile fabrication of a novel visible light active g-C_3N_4-$CoMoO_4$ heterojunction with largely improved photocatalytic performance. *Mater. Lett.* **2020**, *281*, 128661. [CrossRef]
27. Zhu, Z.; Xia, H.; Li, H. Construction of $CoMoO_4$/g-C_3N_4 binary heterojunction photocatalyst with improving photocatalytic performance for ciprofloxacin under visible light. *Diam. Relat. Mater.* **2023**, *133*, 109735. [CrossRef]
28. Xu, S.; Li, M.; Wang, Y.; Jin, Z. Enhanced photocatalytic hydrogen evolution over coal-based carbon quantum dots modified $CoMoO_4$/g-C_3N_4. *Int. J. Hydrogen Energy* **2024**, *51*, 16–30. [CrossRef]
29. Aishwarya, C.S.; Kottam, N.; Savitha, H.; Mahanthappa, M.; Afzal, M. Carbon quantum dot–decorated $CoMoO_4$: A versatile nanohybrid for photocatalytic dye degradation, bifunctional electrocatalysis, and supercapacitor applications. *Inorg. Chem. Commun.* **2026**, *184*, 116019. [CrossRef]
30. Liu, Z.; Xu, J.; Xiang, C.; Liu, Y.; Ma, L.; Hu, L. S-scheme heterojunction based on ZnS/$CoMoO_4$ ball-and-rod composite photocatalyst to promote photocatalytic hydrogen production. *Appl. Surf. Sci.* **2021**, *569*, 150973. [CrossRef]
31. Lu, J.; Liu, T.; Ma, Y.; Luo, K.; Lei, W.; Liu, D. Rational design of bearing-construction nanoreactor for photocatalytic application. *Battery Energy* **2026**, *5*, e70087. [CrossRef]
32. Chu, X.; Sathish, C.I.; Li, M.; Yang, J.-H.; Li, W.; Qi, D.-C.; Chu, D.; Vinu, A.; Yi, J. Anti-Stoke effect induced enhanced photocatalytic hydrogen production. *Battery Energy* **2023**, *2*, 20220041. [CrossRef]
33. Pan, X.; Yang, M.-Q.; Fu, X.; Zhang, N.; Xu, Y.-J. Defective TiO_2 with oxygen vacancies: Synthesis, properties and photocatalytic applications. *Nanoscale* **2013**, *5*, 3601–3614. [CrossRef]
34. Sing, K.S.W.; Everett, D.H.; Haul, R.A.W.; Moscou, L.; Pierotti, R.A.; Rouquérol, J.; Siemieniewska, T. Reporting physisorption data for gas/solid systems with special reference to the determination of surface area and porosity. *Pure Appl. Chem.* **1985**, *57*, 603–619. [CrossRef]
35. Tauc, J.; Grigorovici, R.; Vancu, A. Optical properties and electronic structure of amorphous germanium. *Phys. Status Solidi B* **1966**, *15*, 627–637. [CrossRef]
36. Houas, A.; Lachheb, H.; Ksibi, M.; Elaloui, E.; Guillard, C.; Herrmann, J.-M. Photocatalytic degradation pathway of methylene blue in water. *Appl. Catal. B Environ.* **2001**, *31*, 145–157. [CrossRef]
37. Suyana, P.; Sneha, K.R.; Nair, B.N.; Karunakaran, V.; Mohamed, A.P.; Warrier, K.G.K.; Hareesh, U.S. A facile one pot synthetic approach for C_3N_4–ZnS composite interfaces as heterojunctions for sunlight-induced multifunctional photocatalytic applications. *RSC Adv.* **2016**, *6*, 17800–17809. [CrossRef]
38. Qin, Y.L.; Zhao, W.W.; Sun, Z.; Liu, X.Y.; Shi, G.L.; Liu, Z.Y.; Ni, D.R.; Ma, Z.Y. Photocatalytic and adsorption property of ZnS–TiO_2/RGO ternary composites for methylene blue degradation. *Adsorpt. Sci. Technol.* **2019**, *37*, 764–776. [CrossRef]
39. Zhang, Z.; Zou, C.-T.; Yang, Z.-Y.; Yang, S.-J. One-step preparation and photocatalytic activity of Bi_2MoO_6/$CoMoO_4$ embroidery ball structure. *Chin. J. Inorg. Chem.* **2020**, *36*, 1446–1456.
40. Mamiyev, Z.; Balayeva, N.O. Metal Sulfide Photocatalysts for Hydrogen Generation: A Review of Recent Advances. *Catalysts* **2022**, *12*, 1316. [CrossRef]

Disclaimer/Publisher's Note: The statements, opinions and data contained in all publications are solely those of the individual author(s) and contributor(s) and not of MDPI and/or the editor(s). MDPI and/or the editor(s) disclaim responsibility for any injury to people or property resulting from any ideas, methods, instructions or products referred to in the content.